A numerical homogenization scheme used for derivation of a homogenized viscoelastic-viscoplastic model for the transverse response of fiber-reinforced polymer composites

Liu, Y.; van der Meer, F.P.; Sluys, L.J.; Fan, J. T.

DOI
10.1016/j.compstruct.2020.112690

Publication date
2020

Document Version
Accepted author manuscript

Published in
Composite Structures

A numerical homogenization scheme used for derivation of a homogenized viscoelastic-viscoplastic model for the transverse response of fiber-reinforced polymer composites

Y. Liu[a,b], F.P. van der Meer[b], L.J. Sluys[b], J.T. Fan[a,*]

[a] State Key Laboratory of Explosion Science and Technology, Beijing Institute of Technology, Beijing, 100081, China
[b] Faculty of Civil Engineering and Geosciences, Delft University of Technology, PO Box 5048, 2600 GA Delft, The Netherlands

Abstract

With a classical notched configuration, the damage process in the transverse plane of fiber-reinforced polymer composites are studied by a direct numerical simulation model (DNS). However, to avoid high computational costs the region in which the fiber/matrix microstructure is explicitly modeled must remain small. Therefore, away from the notch tip, a homogenized model is needed to capture the far-field mechanical response without damage but with possibly rate-dependent nonlinearity. In this contribution, with a representative volume element (RVE), a step-by-step numerical homogenization procedure is introduced to calibrate a homogenized viscoelastic-viscoplastic (VE-VP) model with the same formulation as the VE-VP model used for describing the polymer behavior in the RVE model. The calibrated VE-VP model is used in a homogenized FEM model to describe the composite material response and compared against the RVE model. It is found that: (1) the homogenized model captures the viscoelastic deformation, the rate-dependent yielding, stress relaxation and unloading behavior of the polymer composite well, although the assumptions of a single plastic Poisson's ratio and pure isotropic hardening are oversimplifications of the composite behavior; (2) the novel step-by-step numerical homogenization procedure provides an efficient and accurate way for obtaining material parameters of a VE-VP model.

Keywords: Composites, Viscoelasticity, Viscoplasticity, RVE, Numerical homogenization

1. Introduction

Fiber-reinforced polymer composites exhibit a complex nonlinear mechanical response in the transverse plane, due to the composition of different types of materials and interfaces between the constituents. By modeling the composite microstructure with a fine numerical model, a virtual testing tool can be established to evaluate the damage and failure of composites in the transverse plane for given constituents and material interfaces instead of performing expensive experiment campaigns. For detailed analysis of crack growth, a direct numerical simulation (DNS) model with a notched configuration is useful as it mimics a typical material characterization experiment. To reduce the computational cost, the composite material away from the notch can be represented by a homogenized model without damage and failure but with possibly rate-dependent nonlinearity. Experimental tests of polymer composites under different loading types, such as fatigue, impact, etc., reveal that polymer composites can show evident viscoelastic deformation and viscoplastic flow before damage and failure emerge [1–3]. The underlying mechanism of the viscoelastic and viscoplastic behavior of polymer composites is related to the nonlinear and time-dependent mechanical properties of the microstructure [4]. Various homogenization strategies exist to calculate the effective properties of polymer composites based on the mechanical properties of the microstructural constituents [5]. The homogenization methods can be divided roughly into: mean-field homogenization, mathematical (asymptotic) homogenization, computational homogenization and numerical homogenization [6, 7].

*Corresponding author
Email address: jitang_fan@bit.edu.cn (J.T. Fan)

The mean field homogenization method was first proposed for composites having linear elastic constituents. It is based on assumed relations between volume averages of strain fields in each phase. This relation is typically derived from the exact solution of Eshelby [8] for an ellipsoidal inclusion embedded in an infinite matrix or its extensions with consideration of multiple inclusions by Mori and Tanaka [9], self-consistent scheme by Kröner [10] and Hill [11], and double inclusion schemes [5]. Extension of these schemes to the nonlinear (time-dependent) regime usually requires the linearization of the local constitutive equations and the definition of uniform reference properties for each phase. Popular linearization strategies include secant [12], incremental [13], tangent [14] and affine [15–17] approaches. Examples of the application of mean field homogenization for nonlinear (elasto-plastic, viscoelastic, elasto-visco-plastic) mechanical problems can be found in [15, 18–21]. This semi-analytical method can be very accurate in linear (thermo)elasticity and it is computationally efficient. However, there is no detailed stress/strain field for each phase and accurate extension to nonlinear cases is still challenging.

The mathematical homogenization method represents the physical fields in a composite by asymptotic expansion in powers of a small parameter ζ, which is the ratio of a characteristic size of the heterogeneities and a measure of the macrostructure. The asymptotic expansion allows a decomposition of the final solution into a series of governing equations, which can be evaluated successively from a sequence of (initial) boundary-value problems within a unit cell (or representative volume element) domain. The effective properties are obtained through volume averaging operations [22]. This method is mathematically elegant and rigorous for a periodic microstructure with linear elastic mechanical properties. However, extension to a nonlinear material response is not straightforward although possible with the transformation field analysis [23]. In this method, the inelastic strain field is considered as given eigenstrains, which can be determined from solving linear problems with eigenstrains. Examples can be found for viscoelasticity [24–26] and for viscoplasticity [27–30]

In the computational homogenization method, also referred to as micro-macro analysis or FE^2 [31], the local macroscopic constitutive response is derived from the solution of a microstructural boundary value problem in a (statistically equivalent) representative volume element (RVE) and information of the microscale is hierarchically passed to the macroscale by bridging laws. The RVE is a characteristic sample of heterogeneous material that should be sufficiently large to involve enough composite micro-heterogeneities in order to be representative, however it should be much smaller than the macroscopic dimensions [32]. This method does not introduce any explicit format of the macroscopic constitutive equations as the macroscopic stress is determined from the mechanical deformation state of the associated RVE. However, the implementation of this method is not readily available in a general-purpose finite element code and the computational cost of this method can be prohibitively high. Computational homogenization has been applied to model, amongst others, viscoelasticity [33–35] and viscoplasticity [36–39].

For the numerical homogenization method, also called unit cell method [31], a macroscopic canonical constitutive law, e.g. viscoplasticity, is assumed a priori for the macroscale model. The material parameters are then determined from the averaged microscopic stress-strain fields calculated from the computational analysis of a microstructural model (a unit cell or an RVE) subjected to fundamental load cases. The calibrated macroscopic constitutive model is then used for modeling composite structures without explicitly representing the microstructure, which greatly reduces the computational cost. When compared with the computational homogenization method, the numerical homogenization does not need to keep solving boundary value problems of RVEs during a macroscale analysis. This approach has been used for development of the so-called homogenization-based or micromechanically derived classical constitutive models, e.g. plasticity and damage [40–42], as well as for viscoleasticity [43, 44] and viscoplasticity [44–46].

In this paper, a viscoelastic-viscoplastic (VE-VP) model for polymer composites is derived using a numerical homogenization scheme. This paper is organized as follows: in Section 2, the basic formulation of the VE-VP model proposed by Rocha et al. [47] is illustrated and the stress update scheme used for implementation of the VE-VP model is introduced. In Section 3, novel step-by-step calibration procedures are introduced to calibrate the material parameters of a homogenized VE-VP model based on the response of a representative volume element (RVE) under typical loading conditions. In Section 4, the performance of the introduced numerical scheme is demonstrated.

2. A viscoelastic-viscoplastic polymer model

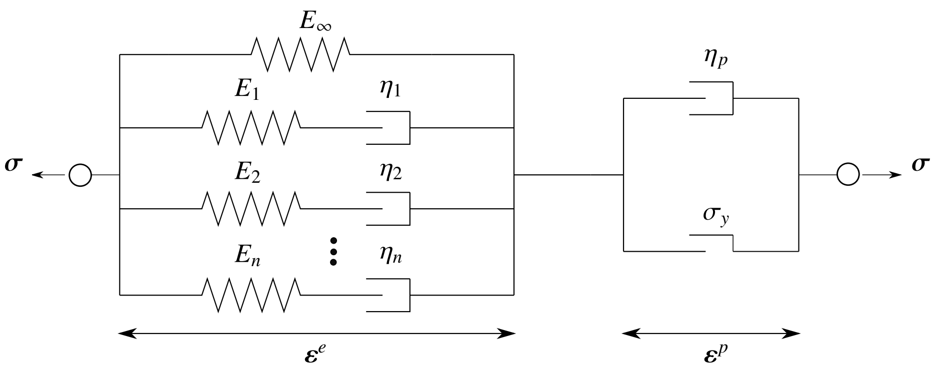

Figure 1: Schematic representation of the viscoelastic-viscoplastic polymer model in one-dimension. The coefficients of the elastic and plastic components do not represent the same coefficients used in Section 2.1.

Following Rocha et al. [47], a viscoelastic-viscoplastic (VE-VP) model as schematically represented in Fig. 1 is used to model the constitutive behavior of an epoxy resin. In this model, the total strain ε_{ij} is decomposed into an elastic part ε^e_{ij} and a plastic part ε^p_{ij}:

$$\varepsilon_{ij} = \varepsilon^e_{ij} + \varepsilon^p_{ij} \tag{1}$$

The elastic behavior is represented by a generalized Maxwell model consisting of n parallel Maxwell elements connected along with an extra isolated long-term spring. In each Maxwell element, a spring with modulus E_i and a dashpot with viscosity parameter η_i are connected in series. The plastic behavior is represented by a sliding element with yield stress σ_y and a dashpot with viscosity parameter η_p. Overstress is allowed to be developed due to the dashpot component that is placed in parallel to the sliding element. In this section, the mathematical formulation for the viscoelasticity and viscoplasticity model is described first, followed by the stress update scheme used for numerical simulation with the finite element method (FEM).

2.1. Formulation for the VE-VP model

Following the conceptual representation of the VE-VP model, the mathematical formulations for the VE-VP constitutive model in a three-dimensional setting is detailed in this section. The contribution of the viscoelastic components is described with a linear viscoelastic model. Afterwards, the viscoplastic components are represented by a Perzyna-type overstress formulation with a backbone of a pressure-dependent plasticity model.

2.1.1. Viscoelasticity

Assuming a linear viscoelastic model, the stress is computed with Boltzmann's hereditary integral related to the elastic strain by [48]:

$$\sigma_{ij}(t) = \int_{-\infty}^{t} D_{ijkl}(t-\tilde{t}) \frac{\partial \varepsilon^e_{kl}(\tilde{t})}{\partial \tilde{t}} d\tilde{t} \tag{2}$$

in which $D_{ijkl}(t)$ is the time-dependent stiffness that can be expressed with the time-dependent shear stiffness $G(t)$ and bulk stiffness $K(t)$:

$$D_{ijkl}(t) = 2G(t) I^{dev}_{ijkl} + 3K(t) I^{vol}_{ijkl} \tag{3}$$

where $G(t)$ and $K(t)$ can be further expanded as an addition of a long-term contribution and a Prony series of n_s shear elements and n_r bulk elements:

$$G(t) = G_\infty + \sum_{s=1}^{n_s} G_s \exp\left(-\frac{t}{g_s}\right) \qquad K(t) = K_\infty + \sum_{r=1}^{n_r} K_r \exp\left(-\frac{t}{k_r}\right) \tag{4}$$

in which G_∞ and K_∞ represent the long-term shear and bulk stiffness, and G_s , K_r, g_s and k_r are shear and bulk stiffness and relaxation time of the Maxwell elements, respectively. The fourth-order deviatoric and volumetric operator tensors introduced in Eq. (3) are defined as:

$$I^{dev}_{ijkl} = \delta_{ik}\delta_{jl} - \frac{1}{3}\delta_{ij}\delta_{kl} \qquad I^{vol}_{ijkl} = \frac{1}{3}\delta_{ij}\delta_{kl} \tag{5}$$

where δ_{ij} is the Kronecker delta. These operator tensors can also be used to decompose the elastic strain ε^e_{ij} into a deviatoric part $\varepsilon^{e,dev}_{ij}$ and a hydrostatic part $\varepsilon^{e,vol}_{ij}$:

$$\varepsilon^e_{ij} = \varepsilon^{e,dev}_{ij} + \varepsilon^{e,vol}_{ij} = I^{dev}_{ijkl}\varepsilon^e_{kl} + I^{vol}_{ijkl}\varepsilon^e_{kl} \tag{6}$$

By substituting Eqs. (4) into Eq. (3), the time-dependent stiffness $D_{ijkl}(t)$ can be expressed as:

$$D_{ijkl}(t) = \left(2G_\infty I^{dev}_{ijkl} + 3K_\infty I^{vol}_{ijkl}\right) + \left(\sum_{s=1}^{n_s} 2G_s \exp\left(-\frac{t}{g_s}\right) I^{dev}_{ijkl} + \sum_{r=1}^{n_r} 3K_r \exp\left(-\frac{t}{k_r}\right) I^{vol}_{ijkl}\right) = D^\infty_{ijkl} + D^m_{ijkl}(t) \tag{7}$$

where D^∞_{ijkl} is the long-term stiffness and $D^m_{ijkl}(t)$ is the overall stiffness of the Maxwell elements.

2.1.2. Viscoplasticity

The viscoplasticity model is a Perzyna-type model with a backbone of a hardening plasticity model. Following Rocha et al. [47], the yield function is pressure-dependent and is defined as:

$$f_p(\boldsymbol{\sigma}, \varepsilon^p_{eq}) = 6J_2 + 2I_1(\sigma_c - \sigma_t) - 2\sigma_c\sigma_t \tag{8}$$

where $I_1 = \sigma_{kk}$ is the first stress invariant, $J_2 = \frac{1}{2}S_{ij}S_{ij}$ is the second invariant of the deviatoric stress S_{ij}, and σ_t and σ_c are the yield stress in tension and compression, respectively. The yield stress values σ_t and σ_c are a function of the accumulated equivalent plastic strain ε^p_{eq}, which is in turn related to the plastic strain in an incremental form as:

$$\Delta\varepsilon^p_{eq} = \sqrt{\frac{1}{1+2\nu_p^2}\Delta\varepsilon^p_{ij}\Delta\varepsilon^p_{ij}} \tag{9}$$

in which ν_p is the plastic Poisson's ratio. In case of an applied uniaxial loading along direction-1, the incremental plastic strain in the other two perpendicular directions, i.e. $\Delta\varepsilon^p_{22}$ and $\Delta\varepsilon^p_{33}$, is related to the incremental plastic strain in the loading direction $\Delta\varepsilon^p_{11}$:

$$\Delta\varepsilon^p_{22} = \Delta\varepsilon^p_{33} = -\nu_p\Delta\varepsilon^p_{11} \tag{10}$$

The desired contraction behavior is implemented through a non-associative flow rule which is written in an incremental form as:

$$\Delta\varepsilon^p_{ij} = \Delta\gamma\left(3S_{ij} + \frac{2}{9}\alpha I_1\delta_{ij}\right) \tag{11}$$

where $\Delta\gamma$ is the incremental plastic multiplier and the parameter α is:

$$\alpha = \frac{9}{2}\frac{1-2\nu_p}{1+\nu_p} \tag{12}$$

A viscous time scale is introduced in the model by allowing the overstress to develop beyond the yield surface. The overstress formulation is of Perzyna-type and the evolution of the plastic multiplier $\Delta\gamma$ can therefore be described by:

$$\Delta\gamma = \begin{cases} \frac{\Delta t}{\eta_p}\left(\frac{f_p}{\sigma^0_t\sigma^0_c}\right)^{m_p} & \text{if } f_p > 0 \\ 0 & \text{if } f_p \leq 0 \end{cases} \tag{13}$$

in which σ^0_t and σ^0_c are the yield stress values when $\varepsilon^p_{eq} = 0$, Δt is the time increment, and m_p and η_p are viscoplastic coefficients.

2.2. Stress update scheme

To facilitate the implementation of the introduced VE-VP model in a FEM framework, an incremental stress update scheme and the consistent tangent used for the Newton-Raphson method are derived. The stress update scheme defines how the stress increment $\Delta\sigma_{ij}$ for a material point is related to a strain increment $\Delta\varepsilon_{ij}$, given that all the state variables from the previous time step are known. For each time step a viscoelastic trial stress is always first computed, assuming that the stress development within this step is not beyond the yield surface. Whenever this assumption is violated, a viscoplastic returning-mapping scheme is used to correct the trial stress.

2.2.1. Viscoelastic stress update

Supposing that all the state variables of a material point at time $t = t_n$ are known and applying a strain increment $\Delta\varepsilon_{ij} = \varepsilon_{ij}(t_{n+1}) - \varepsilon_{ij}(t_n)$, the viscoelastic trial stress is derived as follows: a decomposition of the stress into deviatoric part and hydrostatic part gives:

$$\sigma_{ij}(t_{n+1}) = S_{ij}(t_{n+1}) + 3p(t_{n+1})\delta_{ij} \tag{14}$$

in which S_{ij} is the deviatoric stress, p is the hydrostatic stress. By substituting Eqs. (3) and (4) into Eq. (2), the deviatoric and hydrostatic part of the stress at time $t = t_{n+1}$ can be expressed as:

$$S_{ij}(t_{n+1}) = 2G^{\infty}\varepsilon_{ij}^{e,dev}(t_{n+1}) + \sum_{s=1}^{n_s}\int_0^{t_{n+1}} 2G_s \exp\left(-\frac{t_{n+1}-\tilde{t}}{g_s}\right)\frac{\partial\varepsilon_{ij}^{e,dev}(\tilde{t})}{\partial\tilde{t}}d\tilde{t} = 2G^{\infty}\varepsilon_{ij}^{e,dev}(t_{n+1}) + \sum_{s=1}^{n_s}\tau_{ij}^{s}(t_{n+1}) \tag{15}$$

$$p(t_{n+1}) = K^{\infty}\varepsilon_v^e(t_{n+1}) + \sum_{r=1}^{n_r}\int_0^{t_{n+1}} K_r \exp\left(-\frac{t_{n+1}-\tilde{t}}{k_r}\right)\frac{\partial\varepsilon_v^{e}(\tilde{t})}{\partial\tilde{t}}d\tilde{t} = K^{\infty}\varepsilon_v^e(t_{n+1}) + \sum_{r=1}^{n_r}h^{p}(t_{n+1}) \tag{16}$$

in which $\varepsilon_v^e = \varepsilon_{kk}^e$ is the volumetric part of the elastic strain, $\varepsilon_{ij}^{e,dev} = \varepsilon_{ij}^e - \frac{1}{3}\varepsilon_v^e\delta_{ij}$ is the deviatoric part and the viscous components can be described as:

$$\begin{aligned}\tau_{ij}^{s}(t_{n+1}) &= \int_0^{t_{n+1}} 2G_s\exp\left(-\tfrac{t_{n+1}-\tilde{t}}{g_s}\right)\tfrac{\partial\varepsilon_{ij}^{e,dev}(\tilde{t})}{\partial\tilde{t}}d\tilde{t} = \exp\left(-\tfrac{\Delta t}{g_s}\right)\tau_{ij}^{s}(t_n) + 2G_s\left[1-\exp\left(-\tfrac{\Delta t}{g_s}\right)\right]\tfrac{g_s}{\Delta t}\Delta\varepsilon_{ij}^{e,dev}\\ &= \exp\left(-\tfrac{\Delta t}{g_s}\right)\tau_{ij}^{s}(t_n) + 2G_{ve}(\Delta t)\Delta\varepsilon_{ij}^{e,dev}\end{aligned} \tag{17}$$

$$\begin{aligned}h^{p}(t_{n+1}) &= \int_0^{t_{n+1}} K_r\exp\left(-\tfrac{t_{n+1}-\tilde{t}}{k_r}\right)\tfrac{\partial\varepsilon_v^{e}(\tilde{t})}{\partial\tilde{t}}d\tilde{t} = \exp\left(-\tfrac{\Delta t}{k_r}\right)h^{p}(t_n) + K_r\left[1-\exp\left(-\tfrac{\Delta t}{k_r}\right)\right]\tfrac{k_r}{\Delta t}\Delta\varepsilon_v^{e}\\ &= \exp\left(-\tfrac{\Delta t}{k_r}\right)h^{p}(t_n) + K_{ve}(\Delta t)\Delta\varepsilon_v^{e}\end{aligned} \tag{18}$$

with

$$G_{ve}(\Delta t) = G_s\left[1-\exp\left(-\frac{\Delta t}{g_s}\right)\right]\frac{g_s}{\Delta t} \qquad K_{ve}(\Delta t) = K_r\left[1-\exp\left(-\frac{\Delta t}{k_r}\right)\right]\frac{k_r}{\Delta t} \tag{19}$$

By using Eqs. (15)-(19), the stress $\sigma_{ij}(t_{n+1})$ can be expressed as:

$$\begin{aligned}\sigma_{ij}(t_{n+1}) &= S_{ij}(t_{n+1}) + 3p(t_{n+1})\delta_{ij}\\ &= D_{ijkl}^{\infty} : \varepsilon_{kl}^{e}(t_{n+1}) + D_{ijkl}^{ve}(\Delta t) : \Delta\varepsilon_{kl}^{e} + \sigma_{ij}^{hist}(t_n)\end{aligned} \tag{20}$$

with

$$D_{ijkl}^{ve}(\Delta t) = 2G_{ve}(\Delta t)I_{ijkl}^{dev} + 3K_{ve}(\Delta t)I_{ijkl}^{vol} \tag{21}$$

$$\sigma_{ij}^{hist}(t_n) = \sum_{s=1}^{n_s}\exp\left(-\frac{\Delta t}{g_s}\right)\tau_{ij}^{s}(t_n) + 3\sum_{r=1}^{n_r}\exp\left(-\frac{\Delta t}{k_r}\right)h^{p}(t_n)\delta_{ij} \tag{22}$$

For the trial stress it is assumed that there is no plastic strain increment, i.e. $\Delta\varepsilon_{ij}^{p} = 0$ and $\Delta\varepsilon_{ij}^{e} = \Delta\varepsilon_{ij}$. Therefore, by using Eq. (20) the viscoelastic trial stress reads:

$$\sigma_{ij}^{tr} = D_{ijkl}^{\infty} : \varepsilon_{kl}^{e}(t_{n+1}) + D_{ijkl}^{ve} : \Delta\varepsilon_{kl} + \boldsymbol{\sigma}^{hist}(t_n) = D_{ijkl}^{\infty} : \left(\varepsilon_{kl}(t_{n+1}) - \varepsilon_{kl}^{p}(t_n)\right) + D_{ijkl}^{ve}(\Delta t) : \Delta\varepsilon_{kl} + \sigma_{ij}^{hist}(t_n) \tag{23}$$

The viscoelastic stress is then substituted into the yield function in Eq. (8) to check if the yield condition is satisfied. If the yield function is not larger than zero, the stress is equal to the trial stress,

$$\sigma_{ij}(t_{n+1}) = \sigma_{ij}^{tr} \tag{24}$$

Otherwise, the stress has to be corrected with the viscoplastic return-mapping scheme outlined in the next section. The consistent tangent operator needed for iterative solving of the global system of equations is given in Appendix A.

2.2.2. Viscoelastic-viscoplastic stress update

If the yield function for a viscoelastic trial stress in Eq. (8) is larger than zero, a return-mapping scheme is needed. In this case, plastic flow should occur so that $\Delta\varepsilon_{ij}^{p} \neq 0$ and $\Delta\varepsilon_{ij}^{e} = \Delta\varepsilon_{ij} - \Delta\varepsilon_{ij}^{p}$. According to Eq. (20) and Eq. (23), the stress can be expressed as:

$$\sigma_{ij} = \sigma_{ij}^{tr} - \left(D_{ijkl}^{\infty} + D_{ijkl}^{ve}(\Delta t)\right)\Delta\varepsilon_{kl}^{p} = \sigma_{ij}^{tr} - \hat{D}_{ijkl}\Delta\varepsilon_{kl}^{p} \tag{25}$$

in which

$$\hat{D}_{ijkl} = D_{ijkl}^{\infty} + D_{ijkl}^{ve}(\Delta t) \tag{26}$$

Substitution of Eq. (26) and replacing the increment of plastic strain defined in Eq. (11) in Eq. (25) gives:

$$\sigma_{ij}(t_{n+1}) = \sigma_{ij}^{tr} - 6\hat{G}\Delta\gamma S_{ij}(t_{n+1}) - \frac{2}{9}\hat{K}\alpha\Delta\gamma\,(I_1)_{n+1}\,\delta_{ij} \tag{27}$$

where

$$\hat{G} = G_{\infty} + G_{ve}(\Delta t) \qquad \hat{K} = K_{\infty} + K_{ve}(\Delta t) \tag{28}$$

Splitting Eq. (27) into its deviatoric and volumetric components gives:

$$S_{ij}(t_{n+1}) = S_{ij}^{tr} - 6\hat{G}\Delta\gamma S_{ij}(t_{n+1}) \Longleftrightarrow S_{ij}(t_{n+1}) = \frac{S_{ij}^{tr}}{1 + 6\hat{G}\Delta\gamma} = \frac{S_{ij}^{tr}}{\zeta_s} \tag{29}$$

$$p(t_{n+1}) = p^{tr} - \frac{2}{3}\Delta\gamma\hat{K}\alpha I_1 \Longleftrightarrow p(t_{n+1}) = \frac{p^{tr}}{1 + 2\hat{K}\alpha\Delta\gamma} = \frac{p^{tr}}{\zeta_p} \tag{30}$$

in which

$$\zeta_s = 1 + 6\hat{G}\Delta\gamma, \quad \zeta_p = 1 + 2\hat{K}\alpha\Delta\gamma \tag{31}$$

Considering Eqs. (8), (9), (11), (29) and (30), the overstress function in Eq. (13) is only a function of $\Delta\gamma$:

$$\Phi(\Delta\gamma) = \frac{\Delta t}{\eta_p}\left(\frac{f_p}{\sigma_t^0\sigma_c^0}\right)^{m_p} - \Delta\gamma = 0 \tag{32}$$

This equation can be solved by a local Newton-Raphson scheme outlined in Appendix B. After the incremental plastic multiplier $\Delta\gamma$ is obtained, the stress can be computed by a back substitution of its value into Eq. (27). The consistent tangent needed for iterative solution of the system of equations in an implicit FEM framework is given in Appendix B.

3. Numerical homogenization scheme

In this section, a numerical homogenization scheme for deriving a viscoelastic-viscoplastic model for two-phase polymeric composites is introduced. In this method, the mechanical response of the composites is assumed to be an average response of the two different phases of the material. Therefore, by selecting a characteristic sample of the heterogeneous composite microstructure, i.e. the so-called representative volume element (RVE), the overall response of composites can be extracted from homogenization of the response of the RVE (see Fig. 2). In this work, a three-dimensional orthotropic periodic RVE of 5×5 fibers with a volume fraction of 60% is created [1]. The polymer phase

[1] A discrete element method generator called HADES is used to generate a stochastic distribution of the fibers with the diameter $D_f = 5\ \mu$m and a minimum distance between fibers $d_{min} = 0.2\ \mu$m, following the procedures in Liu et al. [49]. After this, a mesh is generated with GMSH [50] for the fibers and the matrix.

of the RVE is assumed to be epoxy and the VE-VP model introduced in Section 2 is adopted with given material parameter values. The fiber, which is usually much stiffer and stronger, is assumed to be linear elastic. Perfect bonding is assumed for the interface between the polymer matrix and fibers. This three-dimensional orthotropic RVE is adopted with only the response of the fiber/matrix microstructure in the transverse plane investigated. For that reason we can use an isotropic material for the homogenized response. This isotropic model will only be valid for the 2D response. We choose to do the calibration in plane stress, because this allows for straightforward identification of parameters of the homogenized VE-VP model. For the 3D RVE simulations, global plane stress conditions are applied with periodic boundary conditions with free contraction in the fiber direction, which means that the average stress in fiber direction is equal to zero. Because the nonlinear response of the composite material can be expected to inherit characteristics of the underlying nonlinear model for the polymer matrix, it is assumed that the overall transverse mechanical response of the composite material can be described with the same VE-VP model as the polymer phase alone. Numerical homogenization requires the parameters of the homogenized VE-VP model to be determined from a calibration process. According to the VE-VP model introduced in Section 2.1, the following set of material parameters needs to be determined through numerical homogenization schemes: (1) elasticity-related: Young's modulus E_∞ and Poisson's ratio ν; (2) viscoelasticity-related: relaxation modulus (i.e. K_r and G_s) and relaxation times (i.e. k_r and g_s); (3) plasticity-related: plastic Poisson's ratio ν_p and hardening curves; (4) viscoplasticity-related: m_p and η_p.

The adopted strategy is a step-by-step calibration process based on different components of the homogenized VE-VP material model: (a) elasticity; (b) viscoelasticity; (c) plasticity; (d) viscoplasticity. The central premise of this paper is that if we have a micromodel with representative geometry and rich constitutive relations for the constituents, we can calibrate an equally rich constitutive law for an equivalent homogeneous material by separately accounting for the influence of the different constitutive ingredients. The calibration procedure is performed for two-dimensional plane stress simulations. A three-dimensional orthotropic RVE with free contraction in fiber direction is adopted to ensure a consistent macroscopic plane stress response.

For each calibration step, only one component of the constitutive model is considered while the others are turned off. In this way, the complexity of coupling different mechanisms is reduced and the material parameters for each component of the homogenized VE-VP model can be calibrated through the corresponding homogenization techniques. Typically, the mechanical response of the RVE model under representative loading conditions is investigated with FEM simulations and the average response of the RVE is considered as the reference exact solution of the homogenized VE-VP model. The value of the material parameters of the homogenized VE-VP model can be determined by matching the averaged RVE response with optimization algorithms. Building upon the parameters calibrated from the previous step, each time a certain number of extra parameters is calibrated by extracting the necessary information from the RVE model during a new calibration step. Finally, the whole set of calibrated parameters of the homogenized VE-VP model is obtained.

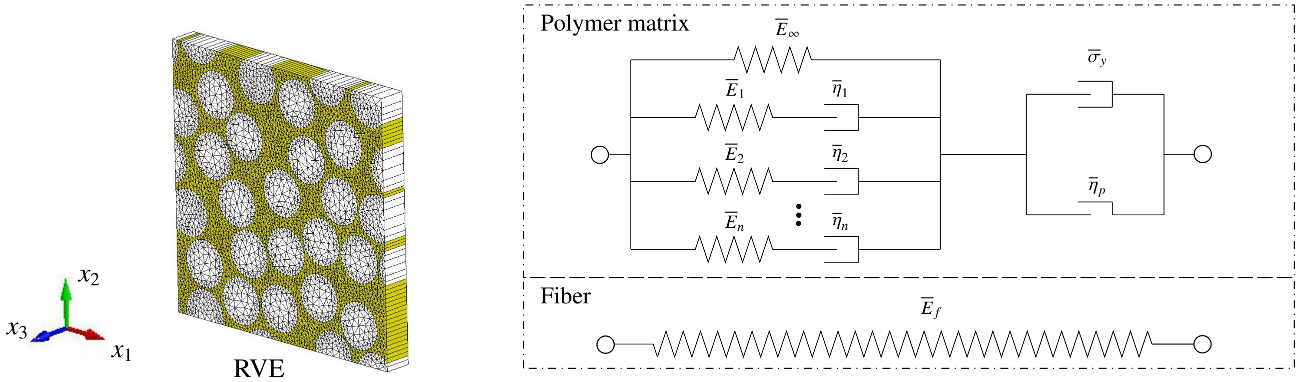

(a) Finite element mesh of the RVE microstructure (the dimensions of the numerical sample are $[l_1, l_2, l_3] = [28.6, 28.6, 0.5]$ μm) and its constitutive models.

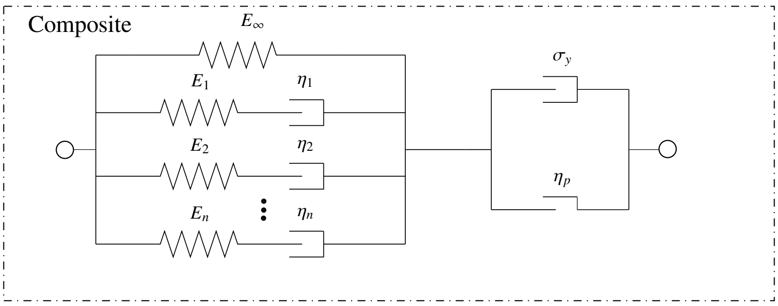

(b) Homogenized VE-VP material model

Figure 2: The equivalent homogeneous model with a VE-VP model (b) is assumed to have the same mechanical behavior as the RVE model with heterogeneous material in (a). The parameters in (b) have to be determined by homogenization of the RVE model.

3.1. Step 1: calibration of elastic component parameters

To calibrate elasticity parameters of the homogenized VE-VP model, only the elasticity components of the RVE model is considered on while the other components are turned off (see Fig. 3). The Young's modulus of the fiber $\overline{E}_f$ and matrix $\overline{E}_\infty$ are 74000 MPa and 2500 MPa, respectively. The Poisson's ratio for fiber $\overline{\nu}_f$ and matrix $\overline{\nu}_m$ are 0.2 and 0.37, respectively. The Young's modulus and Poisson's ratio of the homogenized VE-VP model can be extracted by subjecting the RVE to a uniaxial stress state. The boundary conditions illustrated in Appendix C are applied on the RVE shown in Fig. 3 with a prescribed unit displacement along direction-1. The Poisson's ratio can therefore be calculated as:

$$\nu = -\varepsilon_{22}/\varepsilon_{11} = 0.42 \tag{33}$$

where ε_{22} and ε_{11} are the normal strains along direction-1 and the direction-2, respectively. Similarly, the Young's modulus E_∞ is calculated by:

$$E_\infty = \frac{f_1/(l_2 l_3)}{\varepsilon_{11}} = 10394 \text{ MPa} \tag{34}$$

where f_1 is the total nodal force of the right surface of the RVE model, l_2 and l_3 are the length of the RVE along direction-2 and direction-3, respectively.

3.2. Step 2: calibration of viscoelastic parameters

To calibrate the viscoelastic parameters of the homogenized VE-VP model, only the viscoelastic components of the RVE model are turned on (see Fig. 4). Following [47, 51], a dynamic mechanical analysis (DMA) on the RVE is performed. The basic theory and procedures can be illustrated as follows: it is known that for a viscoelastic material

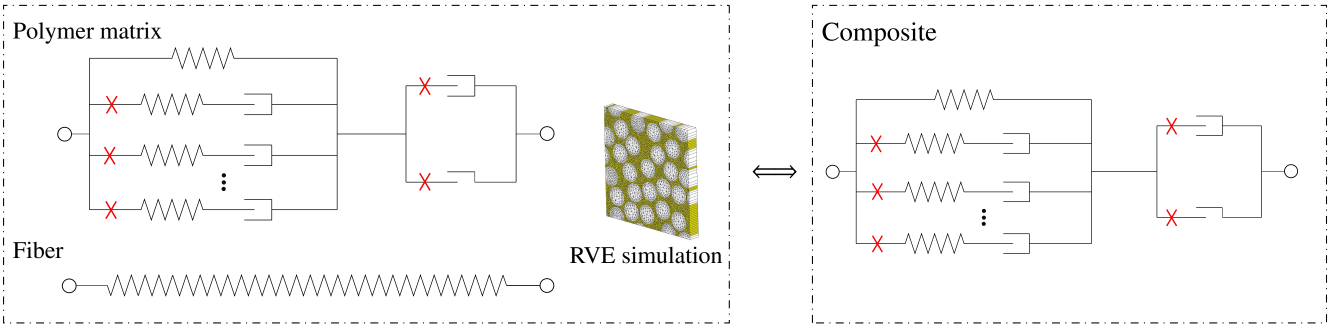

Figure 3: Schematic representation of step 1: the calibration of elasticity parameters of the homogenized VE-VP model. The cross sign represents the components that are turned off.

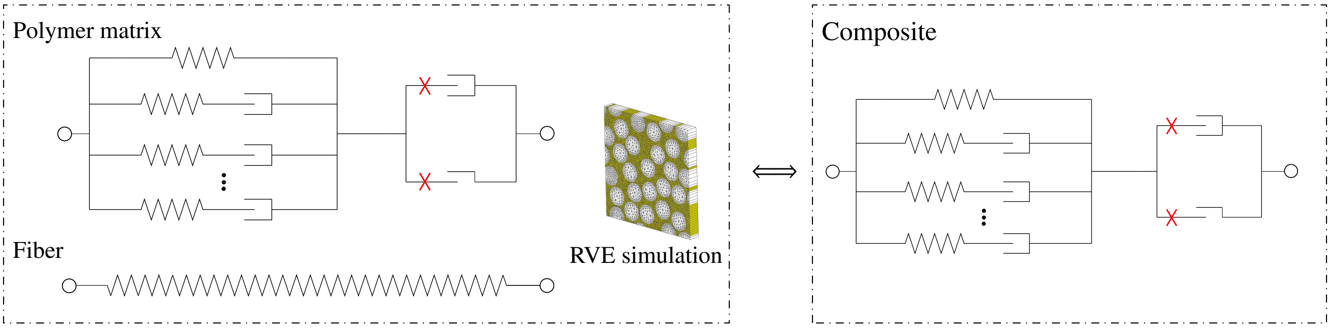

Figure 4: Schematic representation of step 2: the calibration of viscoelasticity parameters of the homogenized VE-VP model. The cross sign represents the components that are turned off.

subjected to a sinusoidal strain $\bar{\varepsilon}^e = \varepsilon_0 \sin(\omega t)$, the resultant stress is also sinusoidal but with a phase shift and can be expressed as:

$$\sigma(t) = \sigma_0 \sin(\omega t + \delta) = E' \varepsilon_0 \sin(\omega t) + E'' \varepsilon_0 \cos(\omega t) \tag{35}$$

where E' is called the storage modulus and E'' is called the loss modulus. Under uniaxial loading, the stress is independent of the Poisson's ratio, and the viscoelastic Young's modulus may be described by a Prony series similar to Eq. (4):

$$E(t) = E_\infty + \sum_{i=1}^{n} E_i \exp\left(-\frac{t}{\tau_i}\right) \tag{36}$$

where E_∞ = 10394 MPa is the long-term Young's modulus which is already calibrated in Section 3.1, E_i and τ_i are the relaxation Young's modulus and the relaxation time for each Maxwell chain, respectively, and n is the number of Maxwell chains. Following Rocha et al. [47], four Prony series are used for the polymer model and the corresponding parameter values are listed in Table 1. For given parameters E_i and τ_i, the stress signal is given as:

$$\sigma(t) = \int_{-\infty}^{t} E(t-\tilde{t}) \frac{\partial \bar{\varepsilon}^e(\tilde{t})}{\partial \tilde{t}} d\tilde{t} = \left(E_\infty + \sum_{i=1}^{4} \frac{E_i \omega^2}{\omega^2 + \frac{1}{\tau_i^2}} \right) \varepsilon_0 \sin(\omega t) + \left(\sum_{i=1}^{4} \frac{E_i \frac{\omega}{\tau_i}}{\omega^2 + \frac{1}{\tau_i^2}} \right) \varepsilon_0 \cos(\omega t) \tag{37}$$

$\overline{\tau}_i$ (ms)	52.7704	2938.8889	5.4080e4	3.9612e7
$\overline{E}_i$ (MPa)	98.5401	142.4348	487.7009	112.2702

Table 1: Prony series parameter values for the polymer model

from which the storage modulus and loss modulus can be identified as:

$$E'(\omega) = E_\infty + \sum_{i=1}^{4} \frac{E_i \omega^2}{\omega^2 + \frac{1}{\tau_i^2}} \tag{38}$$

$$E''(\omega) = \sum_{i=1}^{4} \frac{E_i \frac{\omega}{\tau_i}}{\omega^2 + \frac{1}{\tau_i^2}} \tag{39}$$

The closed-form formulations given in Eq. (38) and Eq. (39) show that both the storage modulus E' and the loss modulus E'' are a function of the applied angular frequency ω.

To calibrate the viscoelastic parameters of the homogenized VE-VP model, 10 DMA simulations with uniaxial tension on the RVE with 10 different angular frequencies $\omega_i \in 2\pi \times [0.05, 0.1, 0.5, 1.0, 2.0, 5.0, 10.0, 15.0, 20.0, 25.0]$ Hz and the same magnitude $\varepsilon_0 = 0.0001$ mm are performed and the overall stress of the RVE is recorded. The boundary conditions illustrated in Appendix C are applied on the RVE shown in Fig. 4 and the overall stress is calculated according to Eq. (63). For each case, the values of E' and E'' can be calculated from the stress of the simulation, considering the closed-form expression Eq. (35). These values for the storage modulus and loss modulus are plotted in Fig. 5. Meanwhile, a nonlinear least-square optimization algorithm implemented in the LSQNONLIN function in MATLAB is used to match the numerical results with the closed-form formulation of E' and E''. The two objective functions that are minimized by running the LSQNONLIN are:

$$y(x) = \begin{bmatrix} \sqrt{\sum_{i=1}^{10} \left(E_i'(\omega_i, x) - \overline{E}_i'(\omega_i)\right)^2} \\ \sum_{i=1}^{10} \left(E_i''(\omega_i, x) - \overline{E}_i''(\omega_i)\right)^2 \end{bmatrix} \tag{40}$$

where $x = (E_1, E_2, E_3, E_4, \tau_1, \tau_2, \tau_3, \tau_4)$ are the unknown viscoelastic relaxation modulus and relaxation times needed to be calibrated, $E_i'(\omega_i, x)$ and $E_i''(\omega_i, x)$ are the relaxation modulus and relaxation time calculated from Eq. (38) and Eq. (39), and $\overline{E}_i'(\omega_i)$ and $\overline{E}_i''(\omega_i)$ are the storage modulus and loss modulus obtained from each RVE simulation. Finally, the calibrated VE parameters are:

$$[E_1, E_2, E_3, E_4, \tau_1, \tau_2, \tau_3, \tau_4]^T = \begin{bmatrix} 256.4811 \\ 188.1201 \\ 2232.8425 \\ 302.9434 \\ 61.1900 \\ 553.0494 \\ 40905.3228 \\ 30015955.2538 \end{bmatrix} \tag{41}$$

By substituting the calibrated values in Eq. (41) into Eq. (38) and Eq. (39), the calibrated loss modulus and storage modulus functions are obtained. The comparison between this calibrated solution and the RVE solution shown in Fig. 5 verifies the accuracy of the calibration procedure.

Next, the relaxation bulk modulus K_i and shear modulus G_i can be obtained by:

$$G_i = \frac{E_i}{2(1+\nu)}, \qquad K_i = \frac{E_i}{3(1-2\nu)}, \qquad i = 1, 2, 3, 4 \tag{42}$$

where $\nu = 0.42$ is the elastic Poisson's ratio calibrated in Section 3.1. The relaxation times for bulk modulus and shear modulus are obtained by [52]:

$$g_i = \frac{E_i \tau_i}{G_i}, \qquad k_i = \frac{E_i \tau_i}{K_i}, \qquad i = 1, 2, 3, 4 \tag{43}$$

All these data are listed in Table 2.

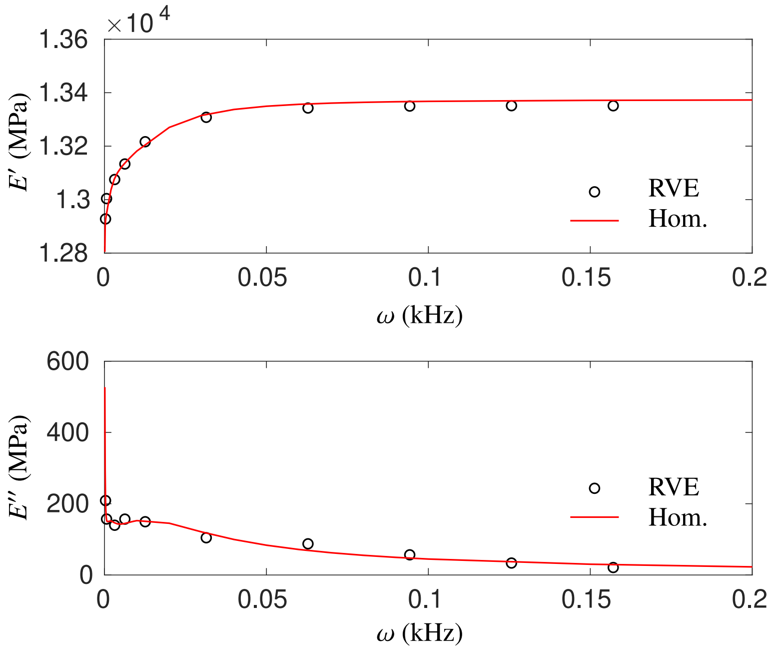

Figure 5: Comparison of storage modulus and loss modulus results between RVE model and the homogenized model with calibrated parameters

G_i (MPa)	90.3102	66.2395	786.2121	106.6702
g_i (ms)	173.7796	1570.6603	116171.1168	85245312.9208
K_i (MPa)	534.3356	391.9169	4651.7552	631.1321
k_i (ms)	29.3712	265.4637	19634.5549	14407658.5218

Table 2: Bulk and shear relaxation modulus and relaxation times of four Prony series

3.3. Step 3: homogenized plasticity model

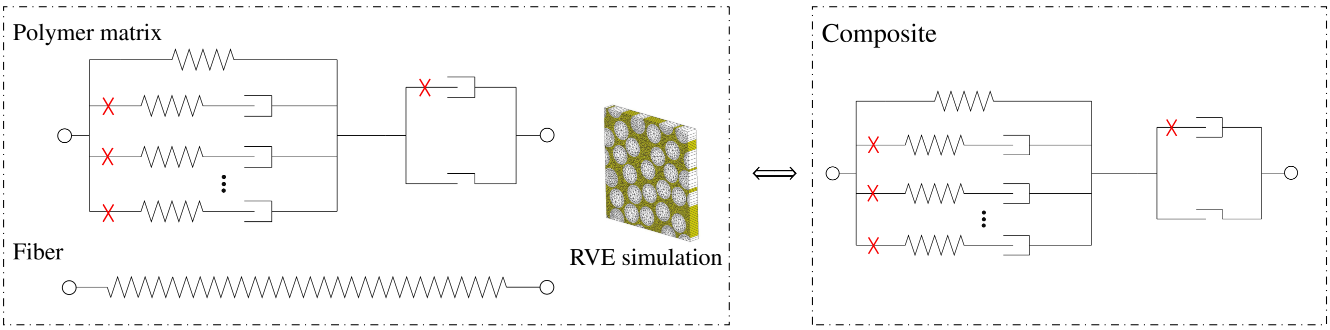

Figure 6: Schematic representation of step 3: the calibration of plasticity parameters of the homogenized VE-VP model. The cross sign represents the components that are turned off.

To calibrate the plasticity properties of the homogenized VE-VP model, i.e. the plastic Poisson's ration ν_p and the hardening curves, only the plasticity components of the RVE model are turned on (see Fig. 6) with the homogenized elasticity properties from Section 3.1. The plastic Poisson's ratio is 0.32 and the hardening curves of the matrix for tension and compression are $\sigma_t\left(\varepsilon_{eq}^p\right) = 64.80 - 33.6\exp\left(-\varepsilon_{eq}^p/0.003407\right) - 10.21\exp\left(-\varepsilon_{eq}^p/0.06493\right)$ and $\sigma_c = 1.25\sigma_t$ (see Fig. 8b). Two types of stress states are applied on the RVE: a uniaxial tensile stress and a uniaxial compressive stress, to account for the hardening plasticity behavior under both tension and compression loading. The boundary conditions illustrated in Appendix C are applied on the RVE shown in Fig. 6 with a tensile (and compressive) loading rate $\dot{\bar{u}}$ of 0.003 m/s.

During the RVE simulation, the average stress σ_{11} and strains ε_{11}, ε_{22} are recorded. The stress vs. strain curve and the distribution of the equivalent plastic strain at several representative time instants of the two cases are shown in Fig. 7. There is an initial linear region where the material is deforming elastically (see point A in Fig. 7). Afterwards, a hardening-type of stress-strain curve is observed while plastic flow occurs and plastic bands start to form (see points B, C, D in Fig. 7). The stress increase in compression is faster than that in tension. From the enclosed subfigures, it can be found that the deformation pattern of the RVE with plastic shear bands is similar to what is expected for a isotropic material under a unidirectional stress state. This verifies the effectiveness of the applied boundary conditions. It should also be noted that the detailed strain and stress field are obtained as well, which is one of the advantages over mean-field homogenization approaches.

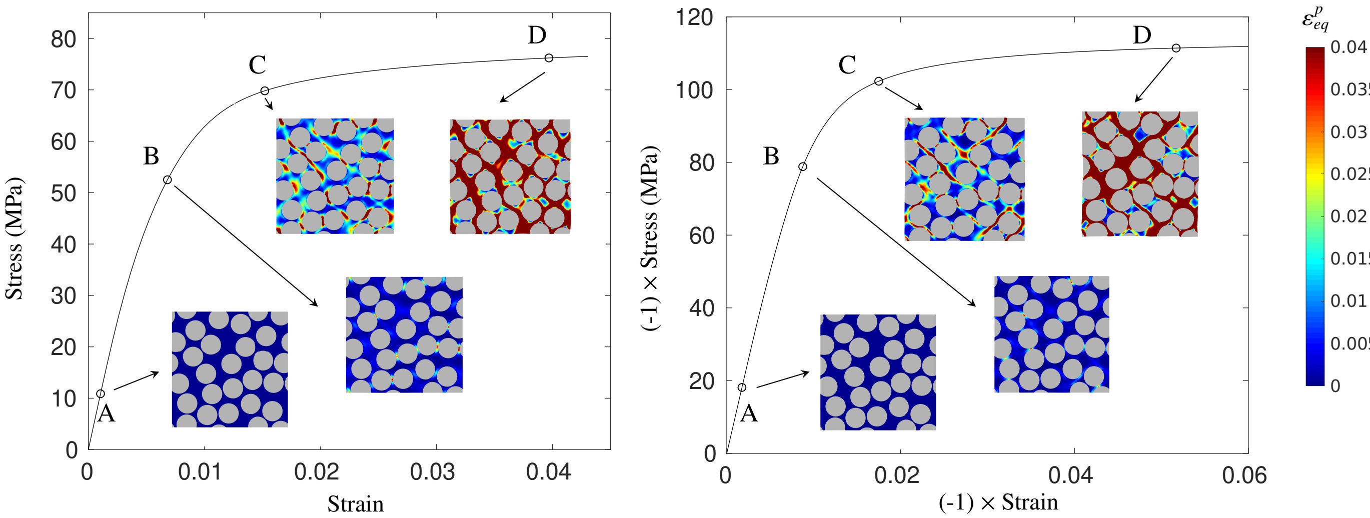

Figure 7: Stress vs. strain curve for tension (left) and compression (right). The enclosed subfigures show the distribution of the equivalent plastic strain ε^p_{eq} for typical time instants.

The plastic Poisson's ratio ν_p for each case can be calculated according to:

$$\nu_p = -\frac{\varepsilon^p_{22}}{\varepsilon^p_{11}} = -\left(\frac{u_2}{l_2} + \nu \cdot \frac{\sigma_{11}}{E_\infty}\right) / \left(\frac{u_1}{l_1} - \frac{\sigma_{11}}{E_\infty}\right) \tag{44}$$

where u_1 and u_2 are the displacement along direction-1 and direction-2, respectively, l_1 and l_2 are the length of RVE along direction-1 and direction-2, respectively, and $\nu = 0.42$ is the elastic Poisson's ratio

The evolution of the plastic Poisson's ratio ν_p with the strain ε_{11} is visualized in Fig. 8. The plastic Poisson's ratio for tension and compression gradually stabilizes to a certain value. For tension that is around 0.34 while for compression it is around 0.5. A similar observation was made in micromechanical simulations by van der Meer [53], showing that the assumption of a single plastic Poisson's ratio is an oversimplification for the composite material response.

In this work, the plastic Poisson's ratio extracted from tensile loading is adopted (i.e. $\nu_p = 0.34$) for simplicity. Therefore, the coefficient α in the flow rule, i.e. Eq. (11), is found to be 1.075. For this transversely isotropic RVE, the definition of the equivalent plastic strain from Eq. (9) is adapted to:

$$\Delta\varepsilon^p_{eq} = \sqrt{\frac{1}{1+\nu_p^2}\Delta\varepsilon^p_{ij}\Delta\varepsilon^p_{ij}} \quad \text{in which } i, j = 1, 2 \tag{45}$$

so that the same in-plane response is found with an isotropic RVE with the equivalent plastic strain defined in Eq. (9). From the unidirectional tension and compression RVE simulations, the hardening curves, i.e. $\sigma_c(\varepsilon_{eq}^p)$ and $\sigma_t(\varepsilon_{eq}^p)$, can be extracted by taking the stress and equivalent plastic strain data pair $(\sigma_{11}^i, \varepsilon_{eq}^p)$ for each time step with:

$$\sigma_{11}^i = \frac{f_1}{l_2 l_3}, \qquad i = c, t \tag{46}$$

The calibrated hardening curves for tension and compression are plotted in Fig. 8(b) along with the hardening curves of the matrix. It is observed that by adding the fibers, the yield stresses increase.

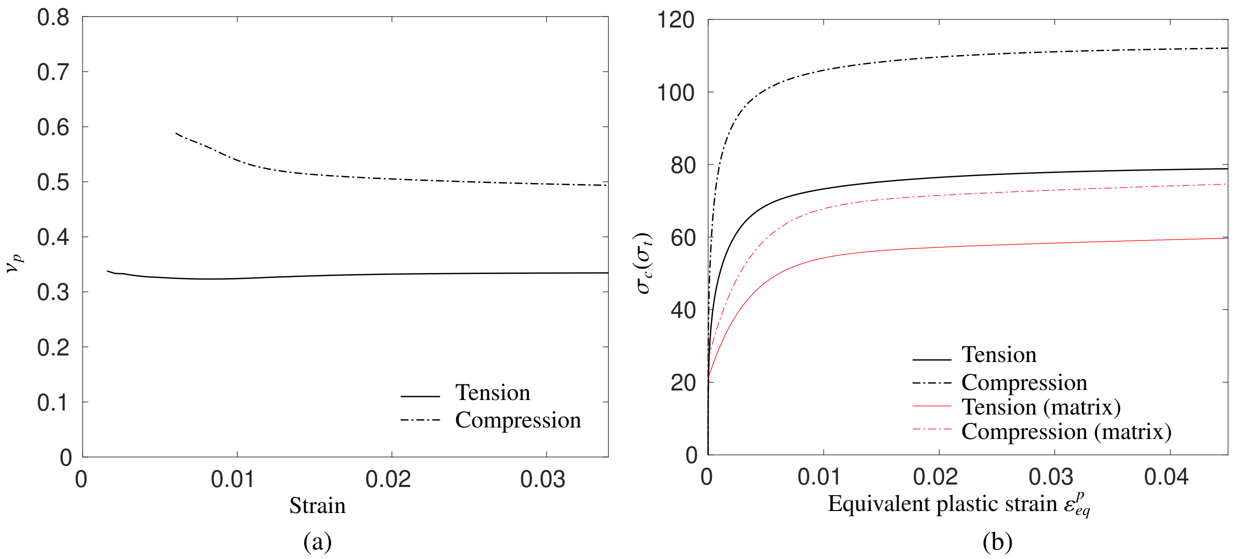

Figure 8: (a) Plastic Poisson's ratio under tension and compression (for the matrix, the plastic Poisson's ratio is 0.32); (b) calibrated hardening curves

3.4. Step 4: homogenized viscoplastic properties

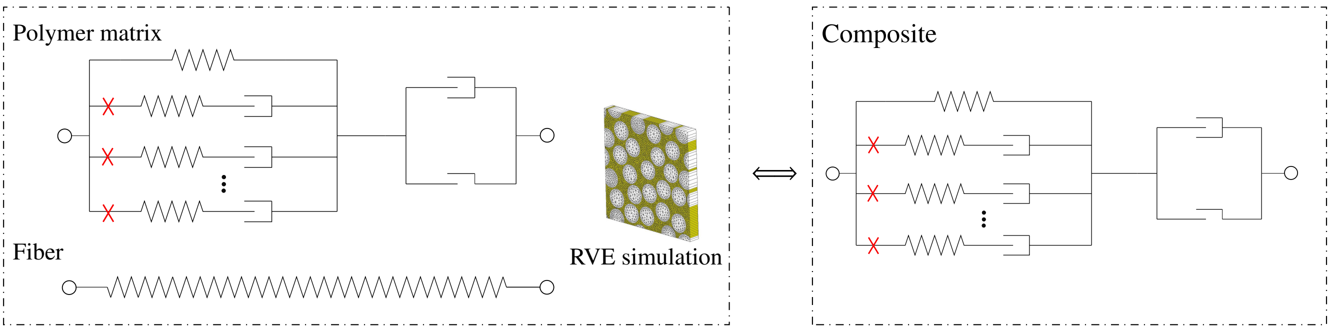

Figure 9: Schematic representation of step 4: the calibration of viscoplasticity parameters of the homogenized VE-VP model. The cross sign represents the components that are turned off.

To obtain the viscoplasticity parameters of the homogenized VE-VP model, i.e. m_p and η_p, part of the polymer and the homogenized model are turned off. The RVE is loaded in unidirectional tension and different loadings are considered. The boundary conditions illustrated in Appendix C are applied on the RVE shown in Fig. 9. The elasticity and plasticity properties of the polymer in the RVE model have already been introduced in Section 3.1 and Section 3.3, respectively. The viscoplastic coefficients for the polymer are $\overline{m}_p = 7.305$ and $\overline{\eta}_p = 3.49 \cdot 10^{12}$ MPa·s. Six different cases with the loading rates $\dot{\varepsilon}_{11} \in [0.00035, 0.00175, 0.0035, 0.0175, 0.035, 0.175]$ s^{-1} are applied on the RVE. The stress-strain relations of the six cases are plotted in Fig. 10. Single element tests with the homogenized VE-VP model are performed to match the six RVE simulation results with given viscoplastic coefficients m_p and η_p. The elasticity and plasticity properties of the homogenized VE-VP model are already calibrated in Section 3.1 and Section 3.3. Therefore, only the homogenized viscoplastic parameters m_p and η_p need to be calibrated. In order to find an optimal combination of these parameters, 7×5 simulations of the homogenized VE-VP model with a combination of one of the seven m_p values and one of the five η_p values listed in Table 3 are performed. Six objective functions are introduced as:

$$y(m_p, \eta_p) = \begin{bmatrix} \sum_{i=1}^{n_1} \left(\Xi_i^{(1)}\left(m_p, \eta_p\right) - \overline{\Xi}_i^{(1)}\right)^2 \\ \sum_{i=1}^{n_2} \left(\Xi_i^{(2)}\left(m_p, \eta_p\right) - \overline{\Xi}_i^{(2)}\right)^2 \\ \sum_{i=1}^{n_3} \left(\Xi_i^{(3)}\left(m_p, \eta_p\right) - \overline{\Xi}_i^{(3)}\right)^2 \\ \sum_{i=1}^{n_4} \left(\Xi_i^{(4)}\left(m_p, \eta_p\right) - \overline{\Xi}_i^{(4)}\right)^2 \\ \sum_{i=1}^{n_5} \left(\Xi_i^{(5)}\left(m_p, \eta_p\right) - \overline{\Xi}_i^{(5)}\right)^2 \\ \sum_{i=1}^{n_6} \left(\Xi_i^{(6)}\left(m_p, \eta_p\right) - \overline{\Xi}_i^{(6)}\right)^2 \end{bmatrix} \tag{47}$$

where $\overline{\Xi}_i^{(k)}$ is the stress of each time increment in each loading rate case $k = 1, 2, ..., 6$ obtained from the RVE simulation, $\Xi_i^{(k)}\left(m_p, \eta_p\right)$ denotes the stress of the homogenized numerical model for the same time increment as the RVE simulation with the value of m_p and η_p, and n_k is the number of time increments for each loading rate case. Afterwards, the function $\Xi_i^{(k)}\left(m_p, \eta_p\right)$ is defined by the following interpolation/extrapolation scheme:

$$\Xi_i^{(k)}\left(m_p, \eta_p\right) = \sum_{s=1}^{2} \sum_{t=1}^{2} N_s(m_p) N_t(\eta_p) \Xi_i^{(k)}\left(m_p^s, \eta_p^t\right), \qquad m_p^s \in \mathcal{M}, \eta_p^t \in \mathcal{Q} \tag{48}$$

where $N_s(m_p)$ and $N_t(\eta_p)$ are 1st-order Lagrange interpolation functions of m_p and η_p, respectively, and $\Xi_i^{(k)}\left(m_p^s, \eta_p^t\right)$ is the stress of the homogenized numerical model for each loading rate case at the same time increment as the RVE simulation for $m_p^s \in \mathcal{M}$ and $\eta_p^t \in \mathcal{Q}$. By running the LSQNONLIN function in MATLAB, the optimal values of m_p and η_p are found to be $m_p = 6.66$, $\eta_p = 1.2 \cdot 10^{13}$ MPa·s. The stress-strain curves for the homogenized numerical model using the calibrated values are plotted in Fig. 10. It is shown that the homogenized model solution matches very well with the RVE simulation results for the studied strain rate ranges.

$\mathcal{M}$	6.5	6.6	6.7	6.8	6.9	7.0	7.1
$\mathcal{Q}$ (MPa·s)	5.e12	7.e12	1.e13	2.e13	5.e13		

Table 3: A list of all the m_p and η_p values used in homogenized model

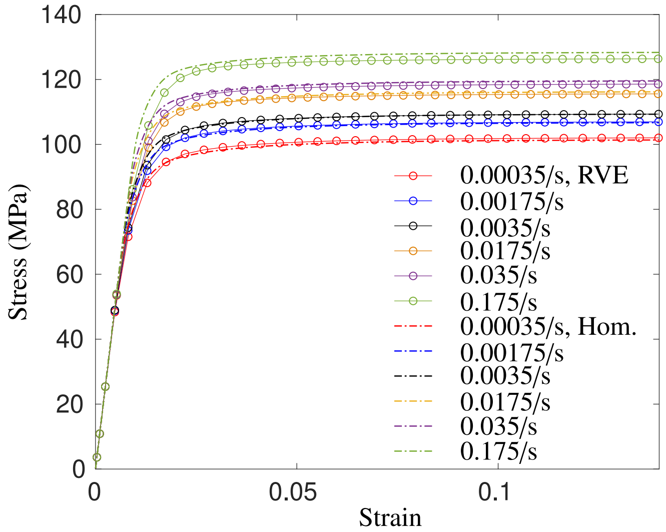

Figure 10: Comparison of Stress-strain relation of monotonic loading for six different strain rates between RVE simulation and the homogenized numerical model

4. Validation

To validate the step-by-step calibration scheme introduced in the previous section, the performance of the homogenized VE-VP model is compared with the RVE model under a number of characteristic loading conditions.

4.1. Rate dependence

The complete homogenized VE-VP model with calibrated parameters from Section 3 is now compared against the RVE simulation for a monotonic loading at different rates. All viscoelasticity and viscoplasticity components are turned on for both the homogenized model and the polymer model in the RVE. Both the homogenized model and the RVE model are loaded in unidirectional tension and two different strain rates are considered: 0.00035/s and 0.175/s. The boundary conditions and the calculation of the overall stress illustrated in Appendix C are applied on both models. The comparison in stress vs. strain relation between the RVE model and the homogenized model for these two strain rates is shown in Fig. 11. For both cases, an extra computation with the homogenized numerical model but with only the viscoplasticity components turned on is performed and its result is also plotted. For both cases, the response of the composite microstructure is captured very well. This is seen from the good match between the RVE model and the homogenized model with all components turned on. The enclosed subfigure also shows that by turning off the viscoelasticity components, the rate-dependent initial stiffness is not captured correctly in the homogenized model, while the yield stress is still captured well. This verifies that the proposed step-by-step calibration scheme does not lack accuracy due to interaction between the different processes.

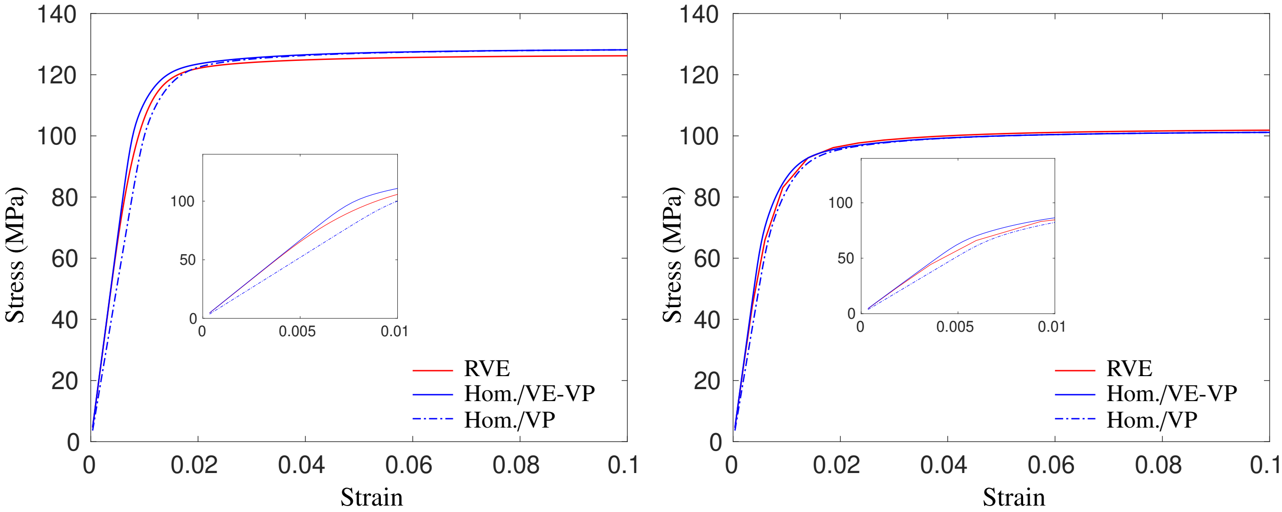

(a) (b)

Figure 11: Comparison of the RVE model and the homogenized model for the stress-strain relation under monotonic loadings. (a) strain rate is 0.175 /s and (b) strain rate is 0.00035/s.

4.2. Loading/unloading/relaxation behavior

To further validate the calibrated parameters m_p and η_p, the cyclic loading cases shown in Fig. 12 are studied. The scenario with loading/unloading (LU) is investigated for two different strain rates: 0.00035/s and 0.175/s. The comparison between the RVE simulation result and the homogenized numerical model is demonstrated in Fig. 13. It is shown that the stress-strain curve for these two cases has a similar pattern, for the first loading/unloading cycle, the stress is first elastic and after the strain is relatively large, viscoplastic flow starts, followed by elastic unloading. Afterwards, in the next loading/unloading cycle, the material is elastically loaded initially and viscoplastic flow continues to develop followed by elastic unloading again. When strain after unloading is relatively large in the last few cycles, plastic flow also starts in compression as observed from the nonlinear part of the unloading branch of the curve. In both cases, the homogenized model matches very well with the RVE model under tension but if compression also happens, there is some deviation where the model would perform better if (part of) the hardening in the homogenized model would be described as kinematic hardening instead of the same isotropic hardening that is present in the matrix model.

Finally, with the loading/relaxation/unloading/relaxation (LRUR) test, the capability of the homogenized model to capture relaxation is investigated. Both the RVE model and homogenized model are loaded in uniaxial tension under a strain rate of 0.0035/s. As shown in Fig. 14, the homogenized numerical model matches very well for both loading and relaxation phases, although again a small deviation is observed for reverse loading when plastic flow in compression starts.

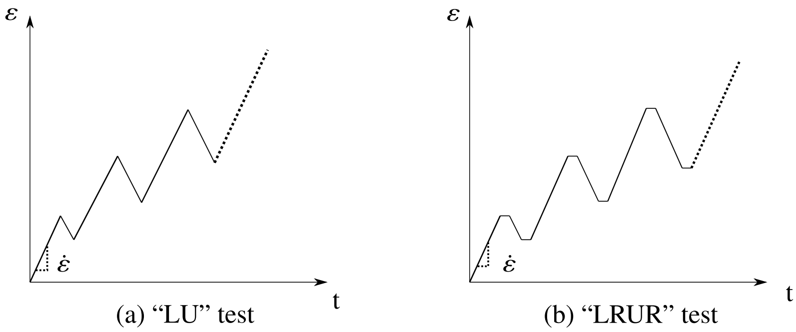

(a) “LU” test (b) “LRUR” test

Figure 12: Two types of periodic-type of loading with constant loading (unloading) rates. (a) Loading/unloading (“LU”) test; (b) Loading/relaxation/unloading/relaxation (“LRUR”) test. The strain rate for the unloading part is the same as the loading part and the unloading stops when the strain is unloaded to 2/3 of the strain when the unloading process starts.

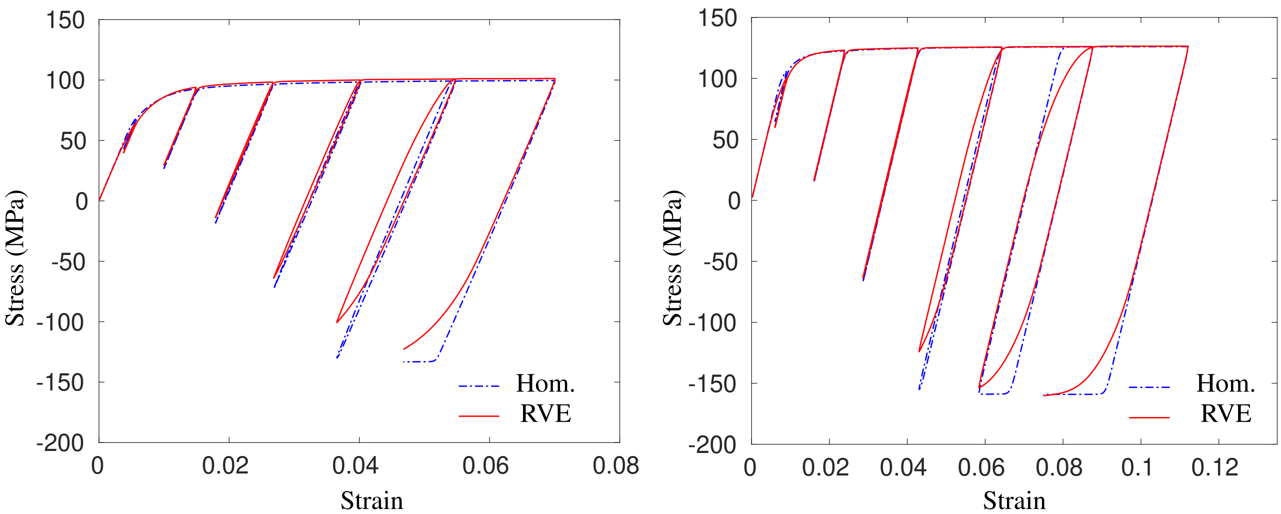

(a) (b)

Figure 13: Comparison of the RVE model and the homogenized model for the stress-strain relation under “LU” loadings. (a) strain rate 0.00035/s; (b) strain rate 0.175/s.

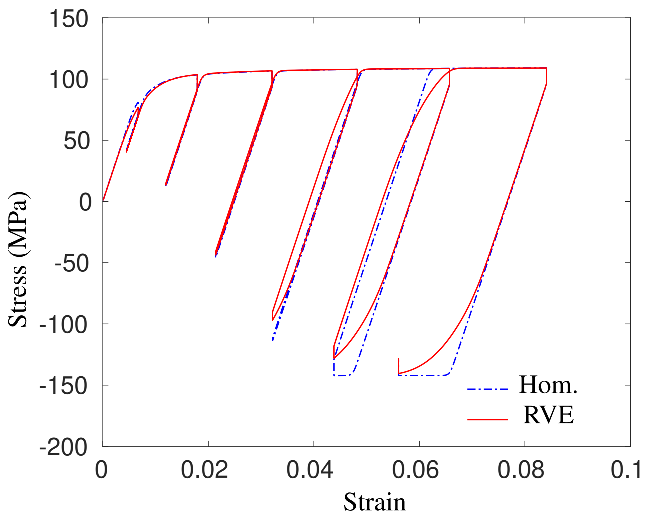

Figure 14: Comparison of the RVE model and the homogenized model for the stress-strain relation under a "LRUR" loading. Strain rate 0.0035/s.

5. Conclusion

In this paper, a numerical homogenization scheme is introduced to derive a viscoelastic-viscoplastic material model for polymer composites. It is assumed that the homogenized VE-VP model has the same formulation as the VE-VP model for the polymeric matrix. The material parameters of different components of the homogenized VE-VP model are calibrated by a novel step-by-step numerical homogenization procedure.

The elasticity properties of the homogenized VE-VP model, including the Young's modulus E_∞ and the elastic Poisson's ration ν, are extracted from the stress and strain in the loading direction and strain in the lateral direction when the RVE model with only the elasticity components turned on is subjected to uniaxial loading. Next, the relaxation modulus and relaxation time of the viscoelastic components of the homogenized VE-VP model are calibrated by performing a series of DMA tests on the RVE model with only viscoelasticity components turned on. A good match of the storage modulus and loss modulus at different loading frequencies between the RVE model and the closed-form solutions in Eq. (38) and Eq. (39) shows that the viscosity of the polymer composites within elastic range is quantified by the calibrated homogenized model accurately. Afterwards, the plastic Poisson's ratio and hardening curves (for both tension and compression) are calibrated by unidirectional load cases with only plasticity components turned on for the RVE model. It is found that the yield stress of the composite is higher than the yield stress of the polymer matrix alone and a single plastic Poisson's ratio is an oversimplification of the polymer composites behavior. The homogenized model with the same isotropic hardening as the matrix model matches very well with the RVE model under monotonic loading. However, if plasticity also happens under reverse loading, there is some deviation where the homogenized model would perform better if (part of) the hardening would be described as kinematic hardening. Next, by turning on the viscoplasticity components of the RVE model, the viscoplasticity related parameters m_p and η_p of the homogenized VE-VP model are calibrated by a series of monotonic tensile tests at different loading rates.

With the calibrated material parameters from the step-by-step numerical homogenization scheme, the homogenized numerical model is compared with the RVE model under characteristic load cases. The capabilities of the homogenized VE-VP model in capturing rate-dependence, loading/unloading and stress relaxation are examined. A good match between these two models demonstrates that the introduced step-by-step numerical homogenization procedure with turning on/off certain components of the material models provides an efficient and accurate way for obtaining material parameters of a VE-VP model. The procedure has been demonstrated for the transverse response of fiber-reinforced composites but can also be used for particle reinforced composites with an appropriate geometry for the RVE.

Acknowledgement

The financial support from the China Scholarship Council (CSC) is gratefully acknowledged by YL. JF acknowledges the financial support from the Fundamental Research Funds for the Central Universities, the independent Research Project of State Key Laboratory of Explosion Science and Technology with Grant No. QNKT20-02, the National Natural Science Foundation of China with Grant No. 11602024, and the "111" Project of China with Grant No. G20012017001.

Appendix A

According to Eq. (20),

$$\sigma_{ij}(t_{n+1}) = D^{\infty}_{ijkl} : \varepsilon^{e}_{kl}(t_{n+1}) + D^{ve}_{ijkl}(\Delta t) : \Delta\varepsilon^{e}_{kl} + \sigma^{hist}_{ij}(t_n) \tag{49}$$

By taking the derivative of the stress $\sigma_{ij}(t_{n+1})$ with respect to the strain $\varepsilon^{e}_{kl}(t_{n+1})$, the consistent tangent can be derived as:

$$D^{con}_{ijkl} = \frac{\partial\sigma_{ij}(t_{n+1})}{\partial\varepsilon_{kl}(t_{n+1})} = \frac{\partial\sigma_{ij}(t_{n+1})}{\partial\varepsilon^{e}_{kl}(t_{n+1})} = D^{\infty}_{ijkl} + D^{ve}_{ijkl}(\Delta t) \tag{50}$$

Appendix B

To solve the local return-mapping scheme, a Newton-Raphson scheme is adopted. Herein, a consistent tangent for the local Newton-Raphson scheme is derived by using:

$$\frac{\partial\Phi}{\partial\Delta\gamma} = \hat{V}\frac{\partial f_p}{\partial\Delta\gamma} - 1 \tag{51}$$

where

$$\hat{V} = \frac{m_p\Delta t}{\eta_p\sigma^0_t\sigma^0_c}\left(\frac{f_p}{\sigma^0_t\sigma^0_c}\right)^{m_p-1} \qquad \frac{\partial f_p}{\partial\Delta\gamma} = -\frac{72\hat{G}J^{\mathrm{tr}}_2}{\zeta^3_s} - \frac{4\left(\sigma_{\mathrm{c}}-\sigma_{\mathrm{t}}\right)\hat{K}\alpha I^{\mathrm{tr}}_1}{\zeta^2_p} + \hat{H}\frac{\partial\Delta\varepsilon^{\mathrm{p}}_{eq}}{\partial\Delta\gamma} \tag{52}$$

with

$$\hat{H} = \frac{\partial f_p}{\partial\varepsilon^p_{eq}} = \frac{2I^{tr}_1}{\zeta_p}\left(\frac{\partial\sigma_c}{\partial\varepsilon^p_{eq}} - \frac{\partial\sigma_t}{\partial\varepsilon^p_{eq}}\right) - 2\left(\sigma_c\frac{\partial\sigma_t}{\partial\varepsilon^p_{eq}} + \sigma_t\frac{\partial\sigma_c}{\partial\varepsilon^p_{eq}}\right) \tag{53}$$

$$\frac{\partial\varepsilon^{\mathrm{p}}_{\mathrm{eq}}}{\partial\Delta\gamma} = \sqrt{\frac{1}{1+2\left(\nu_{\mathrm{p}}\right)^2}}\left(\sqrt{\hat{A}} - \frac{\Delta\gamma}{2\sqrt{\hat{A}}}\left(\frac{216\hat{G}J^{\mathrm{tr}}_2}{\zeta^3_s} + \frac{16\alpha^3\hat{K}\left(I^{\mathrm{tr}}_1\right)^2}{27\zeta^3_p}\right)\right) \tag{54}$$

$$\hat{A} = \frac{18J^{tr}_2}{\zeta^2_s} + \frac{4\alpha^2}{27\zeta^2_p}\left(I^{tr}_1\right)^2 \tag{55}$$

Consistent linearization of Eq. (25) gives:

$$\begin{aligned} D^{con}_{ijkl} = \frac{\partial\sigma_{ij}}{\partial\varepsilon_{kl}} = {} & \frac{\widehat{G}}{\zeta_s}\left(\delta_{ik}\delta_{jl} + \delta_{il}\delta_{jk} - \frac{2}{3}\delta_{ij}\delta_{kl}\right) + \frac{\hat{K}}{\zeta_p}\delta_{ij}\delta_{kl} - \frac{72\widehat{V}\widehat{G}^2}{\mu\zeta^4_s}S^{\mathrm{tr}}_{ij}S^{\mathrm{tr}}_{kl} - \frac{36\left(\sigma_c-\sigma_t\right)\widehat{V}\widehat{K}\widehat{G}}{\mu\zeta_p\zeta^2_s}S^{\mathrm{tr}}_{ij}\delta_{kl} \\ & - \frac{8\alpha I^{\mathrm{tr}}_1\widehat{V}\widehat{K}\widehat{G}}{\mu\zeta^2_p\zeta^2_s}\delta_{ij}S^{\mathrm{tr}}_{kl} - \frac{4\alpha I^{\mathrm{tr}}_1\left(\sigma_c-\sigma_t\right)\widehat{V}\widehat{K}^2}{\mu\zeta^3_p}\delta_{ij}\delta_{kl} - \frac{6\widehat{V}\widehat{G}\widehat{H}}{\mu\zeta^2_s}S^{\mathrm{tr}}_{ij}\widehat{E}_{kl} - \frac{2\alpha I^{\mathrm{tr}}_1\widehat{V}\widehat{K}\widehat{H}}{3\mu\zeta^2_p}\delta_{ij}\widehat{E}_{kl} \end{aligned} \tag{56}$$

where

$$\mu = -\frac{\partial\Phi}{\partial\Delta\gamma} \qquad \hat{E}_{ij} = \frac{\partial\varepsilon^{\mathrm{p}}_{\mathrm{eq}}}{\partial\varepsilon_{ij}} = \frac{1}{1+2\nu^2_p}\frac{(\Delta\gamma)^2}{\Delta\varepsilon^{\mathrm{p}}_{\mathrm{eq}}}M_{kl}\frac{\partial M_{kl}}{\partial\varepsilon_{ij}} \tag{57}$$

$$M_{kl} = \frac{3S^{\mathrm{tr}}_{kl}}{\zeta_S} + \frac{2\alpha I^{\mathrm{tr}}_1\delta_{kl}}{9\zeta_p} \qquad \frac{\partial M_{ij}}{\partial\varepsilon_{kl}} = \frac{6G\left(\delta^s_{ijkl} - \frac{1}{3}\delta_{ij}\delta_{kl}\right)}{\zeta_s} + \frac{\frac{2}{3}\alpha K\delta_{ij}\delta_{kl}}{\zeta_p} \tag{58}$$

The meaning of other variables can be found in Section 2. A more detailed derivation has been presented in [47].

Appendix C

Periodic boundary conditions are applied on the RVE. For instance, for a schematic finite element model with four hexagonal elements as shown in Fig. 15, this implies that:

$$\boldsymbol{u}^R - \boldsymbol{u}^L = \boldsymbol{u}^{(2)} - \boldsymbol{u}^{(0)} \tag{59}$$

$$\boldsymbol{u}^U - \boldsymbol{u}^D = \boldsymbol{u}^{(3)} - \boldsymbol{u}^{(0)} \tag{60}$$

$$\boldsymbol{u}^F - \boldsymbol{u}^B = \boldsymbol{u}^{(1)} - \boldsymbol{u}^{(0)} \tag{61}$$

where $\boldsymbol{u}^R$ and $\boldsymbol{u}^L$ are the displacement of any periodic pair of nodes on the right surface and left surface of the numerical model, respectively, $\boldsymbol{u}^U$ and $\boldsymbol{u}^D$ are the displacement of any periodic pair of nodes on the top surface and bottom surface, respectively, $\boldsymbol{u}^F$ and $\boldsymbol{u}^B$ are the displacement of any periodic pair of nodes on the front surface and back surface, respectively, $\boldsymbol{u}^{(0)}$, $\boldsymbol{u}^{(1)}$, $\boldsymbol{u}^{(2)}$, $\boldsymbol{u}^{(3)}$ are the displacement of master nodes {0,1,2,3}, respectively. To ensure that the RVE deformation under unidirectional loading is the same as an isotropic structure under the same loading condition, special care should be taken with respect to the possible shear deformation. The following constraints are applied to prevent possible shear deformation:

$$u_1^{(0)} = u_2^{(0)} = u_3^{(0)} = u_1^{(2)} = u_3^{(2)} = u_1^{(3)} = u_2^{(3)} = u_2^{(1)} = u_3^{(1)} = 0 \tag{62}$$

Following [49, 54],the incremental average stress for each time step can be calculated by:

$$\delta\sigma = \begin{bmatrix} \delta\sigma_{11} \\ \delta\sigma_{22} \\ \delta\sigma_{33} \\ \delta\sigma_{23} \\ \delta\sigma_{31} \\ \delta\sigma_{12} \end{bmatrix} = \frac{1}{V_0} \begin{bmatrix} \tilde{\boldsymbol{H}}_0 & \tilde{\boldsymbol{H}}_1 & \tilde{\boldsymbol{H}}_2 & \tilde{\boldsymbol{H}}_3 \end{bmatrix} \begin{bmatrix} \delta\boldsymbol{f}_0 \\ \delta\boldsymbol{f}_1 \\ \delta\boldsymbol{f}_2 \\ \delta\boldsymbol{f}_3 \end{bmatrix} \tag{63}$$

with

$$\tilde{\boldsymbol{H}}_q = \begin{bmatrix} x_1^{(q)} & 0 & 0 \\ 0 & x_2^{(q)} & 0 \\ 0 & 0 & x_3^{(q)} \\ 0 & \frac{x_3^{(q)}}{2} & \frac{x_2^{(q)}}{2} \\ \frac{x_3^{(q)}}{2} & 0 & \frac{x_1^{(q)}}{2} \\ \frac{x_2^{(q)}}{2} & \frac{x_1^{(q)}}{2} & 0 \end{bmatrix}, \quad q = 0, 1, 2, 3 \tag{64}$$

in which V_0 is the volume of the RVE, $x_i^{(q)}$ and $\delta\boldsymbol{f}_i$ are the coordinate and incremental nodal forces of the four control nodes, respectively.

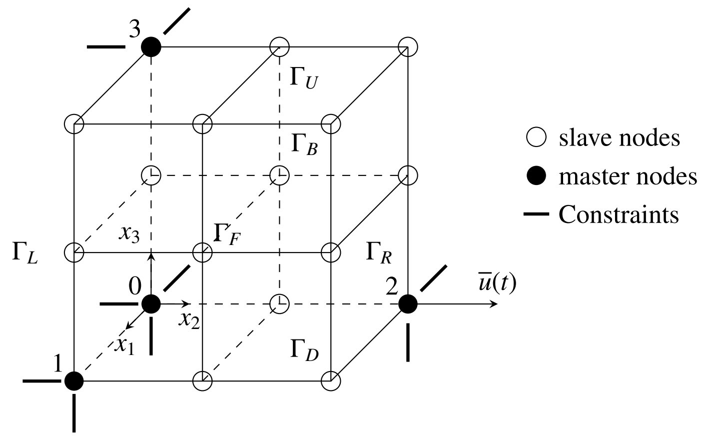

Figure 15: Schematic representation of the periodic and prescribed boundary conditions of a finite element model. Three periodic pairs: top surface Γ_U and bottom surface Γ_D, left surface Γ_L and right surface Γ_R, and front surface Γ_F and back surface Γ_B.

References

[1] T. Schmack, T. Filipe, G. Deinzer, C. Kassapoglou, and F. Walther, "Experimental and numerical investigation of the strain rate-dependent compression behaviour of a carbon-epoxy structure," *Composite Structures*, vol. 189, pp. 256 – 262, 2018.

[2] D. Garcia-Gonzalez, M. Rodriguez-Millan, A. Rusinek, and A. Arias, "Investigation of mechanical impact behavior of short carbon-fiber-reinforced PEEK composites," *Composite Structures*, vol. 133, pp. 1116 – 1126, 2015.

[3] S. V. Thiruppukuzhi and C. T. Sun, "Models for the strain-rate-dependent behavior of polymer composites," *Composites Science and Technology*, vol. 61, no. 1, pp. 1–12, 2001.

[4] M. Shirinbayan, J. Fitoussi, M. Bocquet, F. Meraghni, B. Surowiec, and A. Tcharkhtchi, "Multi-scale experimental investigation of the viscous nature of damage in Advanced Sheet Molding Compound (A-SMC) submitted to high strain rates," *Composites Part B: Engineering*, vol. 115, pp. 3–13, 2017.

[5] S. Nemat-Nasser and M. Hori, *Micromechanics: overall properties of heterogeneous materials*, vol. 37. Elsevier, 2013.

[6] P. Kanouté, D. P. Boso, J. L. Chaboche, and B. A. Schrefler, "Multiscale methods for composites: a review," *Archives of Computational Methods in Engineering*, vol. 16, no. 1, pp. 31–75, 2009.

[7] V. P. Nguyen, M. Stroeven, and L. J. Sluys, "Multiscale continuous and discontinuous modeling of heterogeneous materials: a review on recent developments," *Journal of Multiscale Modelling*, vol. 3, no. 04, pp. 229–270, 2011.

[8] J. D. Eshelby, "The determination of the elastic field of an ellipsoidal inclusion, and related problems," *Proceedings of the Royal Society of London*, vol. 241, no. 1226, pp. 376–396, 1957.

[9] T. Mori and K. Tanaka, "Average stress in matrix and average elastic energy of materials with misfitting inclusions," *Acta Metallurgica*, vol. 21, no. 5, pp. 571–574, 1973.

[10] E. Kröner, "Berechnung der elastischen konstanten des vielkristalls aus den konstanten des einkristalls," *Zeitschrift für Physik*, vol. 151, no. 4, pp. 504–518, 1958.

[11] R. Hill, "A self-consistent mechanics of composite materials," *Journal of the Mechanics and Physics of Solids*, vol. 13, no. 4, pp. 213–222, 1965.

[12] G. P. Tandon and G. J. Weng, "A theory of particle-reinforced plasticity," *Journal of Applied Mechanics*, vol. 55, no. 1, pp. 126–135, 1988.

[13] R. Hill, "Continuum micro-mechanics of elastoplastic polycrystals," *Journal of the Mechanics and Physics of Solids*, vol. 13, no. 2, pp. 89–101, 1965.

[14] A. Molinari, G. R. Canova, and S. Ahzi, "A self consistent approach of the large deformation polycrystal viscoplasticity," *Acta Metallurgica*, vol. 35, no. 12, pp. 2983–2994, 1987.

[15] B. Miled, I. Doghri, L. Brassart, and L. Delannay, "Micromechanical modeling of coupled viscoelastic-viscoplastic composites based on an incrementally affine formulation," *International Journal of Solids and Structures*, vol. 50, no. 10, pp. 1755–1769, 2013.

[16] I. Doghri, L. Adam, and N. Bilger, "Mean-field homogenization of elasto-viscoplastic composites based on a general incrementally affine linearization method," *International Journal of Plasticity*, vol. 26, no. 2, pp. 219–238, 2010.

[17] R. Masson, M. Bornert, P. Suquet, and A. Zaoui, "An affine formulation for the prediction of the effective properties of nonlinear composites and polycrystals," *Journal of the Mechanics and Physics of Solids*, vol. 48, no. 6, pp. 1203 – 1227, 2000.

[18] O. Pierard and I. Doghri, "An enhanced affine formulation and the corresponding numerical algorithms for the mean-field homogenization of elasto-viscoplastic composites," *International Journal of Plasticity*, vol. 22, no. 1, pp. 131–157, 2006.

[19] I. Doghri and C. Friebel, "Effective elasto-plastic properties of inclusion-reinforced composites. Study of shape, orientation and cyclic response," *Mechanics of Materials*, vol. 37, no. 1, pp. 45–68, 2005.

[20] M. Lévesque, K. Derrien, L. Mishnaevski, D. Baptiste, and M. D. Gilchrist, "A micromechanical model for nonlinear viscoelastic particle reinforced polymeric composite materials-undamaged state," *Composites Part A: Applied Science and Manufacturing*, vol. 35, no. 7, pp. 905 – 913, 2004.

[21] R. M. Haj-Ali and A. H. Muliana, "A micromechanical constitutive framework for the nonlinear viscoelastic behavior of pultruded composite materials," *International Journal of Solids and Structures*, vol. 40, no. 5, pp. 1037–1057, 2003.

[22] I. V. Andrianov, V. I. Bolshakov, V. V. Danishevs'kyy, and D. Weichert, "Higher order asymptotic homogenization and wave propagation in periodic composite materials," *Proceedings of the Royal Society A: Mathematical, Physical and Engineering Sciences*, vol. 464, no. 2093, pp. 1181–1201, 2008.

[23] G. J. Dvorak and Y. Benveniste, "On transformation strains and uniform fields in multiphase elastic media," *Proceedings of the Royal Society of London. Series A: Mathematical and Physical Sciences*, vol. 437, no. 1900, pp. 291–310, 1992.

[24] I. V. Andrianov, V. V. Danishevs'kyy, and D. Weichert, "Homogenization of viscoelastic-matrix fibrous composites with square-lattice reinforcement," *Archive of Applied Mechanics*, vol. 81, no. 12, pp. 1903–1913, 2011.

[25] Y.-M. Yi, S.-H. Park, and S.-K. Youn, "Asymptotic homogenization of viscoelastic composites with periodic microstructures," *International Journal of Solids and Structures*, vol. 35, no. 17, pp. 2039 – 2055, 1998.

[26] Q. Li, W. Chen, S. Liu, and J. Wang, "A novel implementation of asymptotic homogenization for viscoelastic composites with periodic microstructures," *Composite Structures*, vol. 208, pp. 276 – 286, 2019.

[27] J. Fish and K. Shek, "Computational plasticity and viscoplasticity for composite materials and structures," *Composites Part B: Engineering*, vol. 29, no. 5, pp. 613 – 619, 1998.

[28] G. Chatzigeorgiou, N. Charalambakis, Y. Chemisky, and F. Meraghni, "Periodic homogenization for fully coupled thermomechanical modeling of dissipative generalized standard materials," *International Journal of Plasticity*, vol. 81, pp. 18–39, 2016.

[29] L. Zhang and W. Yu, "A micromechanics approach to homogenizing elasto-viscoplastic heterogeneous materials," *International Journal of Solids and Structures*, vol. 51, no. 23, pp. 3878 – 3888, 2014.

[30] X. Wu and N. Ohno, "A homogenization theory for time-dependent nonlinear composites with periodic internal structures," *International Journal of Solids and Structures*, vol. 36, no. 33, pp. 4991 – 5012, 1999.

[31] V. Kouznetsova, W. A. M. Brekelmans, and F. P. T. Baaijens, "An approach to micro-macro modeling of heterogeneous materials," *Computational Mechanics*, vol. 27, no. 1, pp. 37–48, 2001.

[32] R. Hill, "Elastic properties of reinforced solids: Some theoretical principles," *Journal of the Mechanics and Physics of Solids*, vol. 11, no. 5, pp. 357 – 372, 1963.
[33] F. V. Souza and D. H. Allen, "Modeling the transition of microcracks into macrocracks in heterogeneous viscoelastic media using a two-way coupled multiscale model," *International Journal of Solids and Structures*, vol. 48, no. 22, pp. 3160 – 3175, 2011.
[34] S. Staub, H. Andrä, M. Kabel, and T. Zangmeister, "Multi-scale simulation of viscoelastic fiber-reinforced composites," *Tech. Mech*, vol. 32, no. 1, pp. 70–83, 2012.
[35] T. Schüler, R. Manke, R. Jänicke, M. Radenberg, and H. Steeb, "Multi-scale modelling of elastic/viscoelastic compounds," *ZAMM-Journal of Applied Mathematics and Mechanics/Zeitschrift für Angewandte Mathematik und Mechanik*, vol. 93, no. 2-3, pp. 126–137, 2013.
[36] F. Feyel and J.-L. Chaboche, "FE^2 multiscale approach for modelling the elastoviscoplastic behaviour of long fibre SiC/Ti composite materials," *Computer Methods in Applied Mechanics and Engineering*, vol. 183, no. 3, pp. 309 – 330, 2000.
[37] R. Berthelsen and A. Menzel, "Computational homogenisation of thermo-viscoplastic composites: Large strain formulation and weak microperiodicity," *Computer Methods in Applied Mechanics and Engineering*, vol. 348, pp. 575–603, 2019.
[38] E. Tikarrouchine, G. Chatzigeorgiou, F. Praud, B. Piotrowski, Y. Chemisky, and F. Meraghni, "Three-dimensional FE^2 method for the simulation of non-linear, rate-dependent response of composite structures," *Composite Structures*, vol. 193, pp. 165–179, 2018.
[39] S. Marfia and E. Sacco, "Multiscale technique for nonlinear analysis of elastoplastic and viscoplastic composites," *Composites Part B: Engineering*, vol. 136, pp. 241 – 253, 2018.
[40] J. R. Brockenbrough, S. Suresh, and H. A. Wienecke, "Deformation of metal-matrix composites with continuous fibers: geometrical effects of fiber distribution and shape," *Acta metallurgica et materialia*, vol. 39, no. 5, pp. 735–752, 1991.
[41] V. Tvergaard, "Analysis of tensile properties for a whisker-reinforced metal-matrix composite," *Acta metallurgica et materialia*, vol. 38, no. 2, pp. 185–194, 1990.
[42] G. Bao, J. W. Hutchinson, and R. M. McMeeking, "Particle reinforcement of ductile matrices against plastic flow and creep," *Acta metallurgica et materialia*, vol. 39, no. 8, pp. 1871–1882, 1991.
[43] A. Courtois, L. Marcin, M. Benavente, E. Ruiz, and M. Lévesque, "Numerical multiscale homogenization approach for linearly viscoelastic 3D interlock woven composites," *International Journal of Solids and Structures*, vol. 163, pp. 61 – 74, 2019.
[44] A. Karamnejad, A. Ahmed, and L. J. Sluys, "A numerical homogenization scheme for glass particle-toughened polymers under dynamic loading," *Journal of Multiscale Modelling*, vol. 08, no. 01, p. 1750001, 2017.
[45] O. van der Sluis, P. J. G. Schreurs, W. A. M. Brekelmans, and H. E. H. Meijer, "Overall behaviour of heterogeneous elastoviscoplastic materials: effect of microstructural modelling," *Mechanics of Materials*, vol. 32, no. 8, pp. 449 – 462, 2000.
[46] O. van der Sluis, P. J. G. Schreurs, and H. E. H. Meijer, "Homogenisation of structured elastoviscoplastic solids at finite strains," *Mechanics of Materials*, vol. 33, no. 9, pp. 499–522, 2001.
[47] I. B. C. M. Rocha, F. P. van der Meer, S. Raijmaekers, F. Lahuerta, R. P. L. Nijssen, and L. J. Sluys, "Numerical/experimental study of the monotonic and cyclic viscoelastic/viscoplastic/fracture behavior of an epoxy resin," *International Journal of Solids and Structures*, vol. 168, pp. 153 – 165, 2019.
[48] S. Haouala and I. Doghri, "Modeling and algorithms for two-scale time homogenization of viscoelastic-viscoplastic solids under large numbers of cycles," *International Journal of Plasticity*, vol. 70, pp. 98–125, 2015.
[49] Y. Liu, F. P. van der Meer, and L. J. Sluys, "A dispersive homogenization model for composites and its RVE existence," *Computational Mechanics*, 2019.
[50] C. Geuzaine and J.-F. Remacle, "Gmsh: A 3-D finite element mesh generator with built-in pre- and post-processing facilities," *International Journal for Numerical Methods in Engineering*, vol. 79, no. 11, pp. 1309–1331, 2009.
[51] A. Krairi and I. Doghri, "A thermodynamically-based constitutive model for thermoplastic polymers coupling viscoelasticity, viscoplasticity and ductile damage," *International Journal of Plasticity*, vol. 60, pp. 163–181, 2014.
[52] B. Miled, I. Doghri, and L. Delannay, "Coupled viscoelastic-viscoplastic modeling of homogeneous and isotropic polymers: Numerical algorithm and analytical solutions," *Computer Methods in Applied Mechanics and Engineering*, vol. 200, no. 47-48, pp. 3381–3394, 2011.
[53] F. P. van der Meer, "Micromechanical validation of a mesomodel for plasticity in composites," *European Journal of Mechanics - A/Solids*, vol. 60, pp. 58–69, 2016.
[54] V. P. Nguyen, O. Lloberas-Valls, M. Stroeven, and L. J. Sluys, "Computational homogenization for multiscale crack modeling. implementational and computational aspects," *International Journal for Numerical Methods in Engineering*, vol. 89, no. 2, pp. 192–226, 2012.